

RESEARCH

Open Access



Corrosion mechanisms for lead-barium glass from the Warring States period

Kexin Zhang^{1,3†}, Jun Wang^{2†}, Wendi Yu¹, Jing Zhao^{1*}, Xuezheng Yue³ and Hongjie Luo¹

Abstract

Lead-barium glass is subject to a variety of corrosion reactions after burial. The microscopic morphology and compositional structure of ancient lead-barium glass excavated from the Yaozhuang Cemetery located in Liuhe District of Nanjing were analysed with optical microscopy, X-ray fluorescence spectrometry, scanning electron microscopy equipped with energy dispersive X-ray spectroscopy, X-ray diffraction, fluorescent inverted microscopy and attenuated total reflectance-Fourier transform infrared spectroscopy. The corrosion products included PbCO_3 , Pb(OH)Cl , $\text{CaHPO}_4(\text{H}_2\text{O})_2$ and BaS_2 . Based on the corrosion morphology and the corrosion products, it was concluded that the corrosion processes included microbial corrosion, surface chemical corrosion, and crack corrosion. This paper describes the corrosion processes of lead-barium glass relics and establishes the corresponding corrosion model. In addition, the results of this study deepen the understanding of the corrosion mechanisms for lead-barium glass and provide new insight into the corrosion mechanisms of excavated glass relics, which is also of great significance for the protection of lead-barium glass.

Keywords Lead-barium glass, Microbial corrosion, Surface chemical corrosion, Crack corrosion, Corrosion model

Introduction

Glass has a long history of development in China that can be traced back thousands of years [1]. China's ancient bronze smelting and refining technology originated in the Shang Dynasty (16th century BC–11th century BC) [2], which increased the development of primitive porcelain technology, when the firing temperatures of proto-porcelain generally reached 1100–1200 °C. In the Western Zhou Dynasty and the early Eastern Zhou Dynasty (the Spring and Autumn), the furnace temperatures could have been higher. When the firing temperature was too

high, the proto-porcelain glaze flowed to form glassy transparent glaze droplets of vitreous material, which may be the earliest ancient glass in China [3]. The excavation sites in China containing lead-barium silicate glass often coincide with the distribution sites of lead ore [4]. The translucent eye beads made of glass, which were excavated in Bozhou, Anhui Province in the Yangtze River Basin, were from the late Spring and Autumn Period and the early Warring States Period (6th–5th century BC) [5], which are the earliest lead-barium silicate glasses found thus far, and lead-barium silicate glass products from the middle and late Warring States Period have been found in the southern and southwestern regions of China [6, 7].

The ancient glass was buried in different environments, which generated a variety of corrosion forms during the burial process; currently, it is generally accepted that the corrosion mechanisms of glass include ion exchange (H^+ /alkali and alkaline earth metal ions) [8, 9]; decomposition and pitting of the Si-O-Si glass skeletal structure [10–13]; hydrolysis of metal ions that make up the various glass

[†]Kexin Zhang and Jun Wang have contributed equally to this work and should be considered co-first authors

*Correspondence:

Jing Zhao

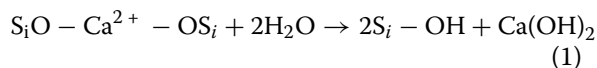
zhaojing@mail.sic.ac.cn

¹ Shanghai Institute of Ceramics, Chinese Academy of Sciences, Shanghai 200050, China

² Nanjing Municipal Institute of Archaeology, Nanjing 210004, China

³ University of Shanghai for Science and Technology, Shanghai 200093, China

networks as well as PbO that makes up the glass intermediates, and one possible hydrolysis reaction is shown in Eq. (1) [14, 15]:



Regarding microbial corrosion of glass, it has been found that ancient glazed tiles were covered by a biological patina composed of microalgae, cyanobacteria, bacteria and some lichenized fungi, some of which penetrated cracks and pores to produce biodegradation [16, 17]. The main effects of biodegradation on historical glass include etching, pitting, leaching, discolouration, glass degradation, gel layer formation and corrosion of the original glass surface [18–21]. The research objects showing microbial corrosion of glass relics are primarily weathered samples, and previous analyses of excavated glass relics have been focused on analysing the chemical compositions of corrosion products, mainly by studying the chemical-physical corrosion processes of cultural relics, but few papers have linked microbial corrosion to the corrosion mechanisms of unearthened artefacts.

Yaozhuang Cemetery located in Liuhe District, Nanjing city, China, was excavated in November 2021, and it is a rectangular vertical pit tomb with a straight wall and a flat bottom. The tomb entrance is 2.54 m long, 1.48 m wide and 2.48 m below the surface. The soil was very wet when the cultural relics were unearthened. Fifteen relics of the Warring States period were cleared, including 12 tombs, 1 chariot pit, 1 pottery figurine pit and 1 utensil pit. The excavated artefacts were mainly pottery combinations such as tripods, beans, Gui, Fang, and cups. In place of the head of the tomb owner in the burial coffin M342 (Fig. 1a, b), a piece of a round artefact with a broken and crispy white surface was

found, which was tentatively identified as aquamarine lead-barium glass from the fracture surface. The soil water content in the excavated area is 24.2%, the pH ranges between 7 and 8, and the electrical conductivity is 47.36 $\mu\text{s}/\text{m}$. Although there was a single artefact sample, the corrosion conditions were diverse and have great research value. Optical microscopy (OM), X-ray fluorescence spectrometry (XRF), scanning electron microscopy equipped with energy dispersive X-ray spectroscopy (SEM-EDX), X-ray diffraction analysis (XRD), fluorescent inverted microscopy (FIM), and attenuated total reflectance-Fourier transform infrared spectroscopy (ATR-FTIR) were utilized to determine the composition and structure of the corroded material on the surfaces of lead-barium glass artefacts, to explore the biological corrosion mechanisms of ancient glass in buried environments, to elaborate the corrosion processes of ancient glass artefacts and to establish a relevant model. The results of the study deepen our understanding of the corrosion mechanisms of ancient lead-barium glass, provide new insight into research on the corrosion mechanisms of excavated glass relics and are also of great significance for the protection of lead-barium glass.

Experimental

Ancient glass sample

Ancient glass fragments excavated from Yaozhuang Cemetery in the Liuhe District of Nanjing were selected as the objects of study. The surface condition of the specific aquamarine corroded glass is shown in Fig. 2, and the surface was covered with a thick corrosion layer. In this paper, the causes of the sample corrosion layer are analysed in detail.

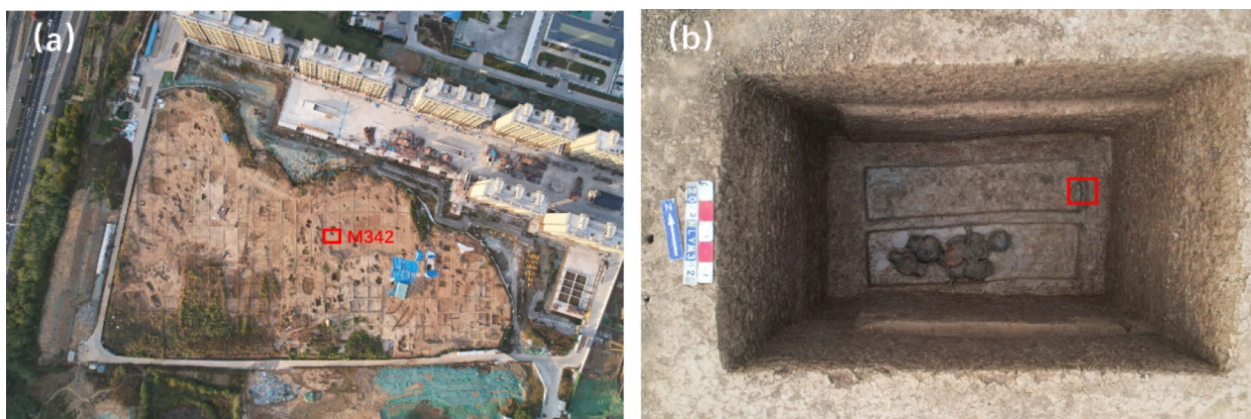


Fig. 1 a Location of the burial site; b location of the sample when it was excavated

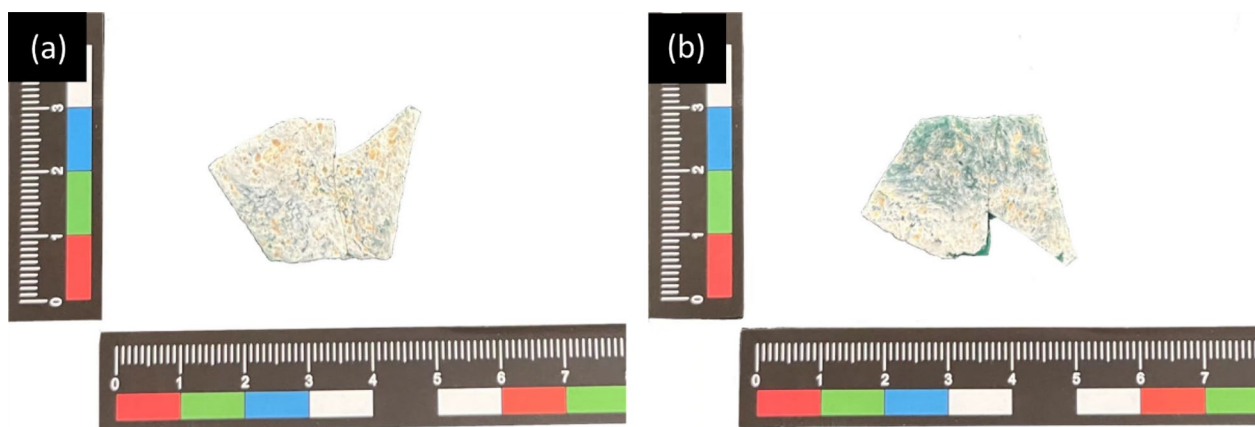


Fig. 2 Photographs of sample morphology, **a** front side with severe corrosion; **b** reverse side

Experimental methods and detection techniques

Optical microscopic analysis (OM)

A 4 K digital microscope (Tianzhu Shanghai optical instrument factory, XTZ-4KHD) was used to observe the morphology of the corrosion layer on the sample surface, and observations were made at magnification levels of 0.7 and 3.5.

X-ray fluorescence spectroscopy (XRF)

A German Bruker M4 Tornado plus microzone X-ray fluorescence imaging spectrometer was used to observe the corrosion layer on the sample surface and test its composition and distribution. XRF is a nondestructive test that only needs a plane without sample preparation and uses an X-ray tube; the target material is Rh, the FP method and type-calibration method are used, and a national standard ore sample is used to establish a quantitative method. The accelerating voltage and beam current were 50 kV and 600 μ A, respectively.

Scanning electron microscopy equipped with energy dispersive X-ray spectroscopy (SEM-EDX)

The FEI Magellan 400 field emission scanning electron microscope/energy spectrum was used to observe the microscopic morphologies of the corroded areas and cross sections of the sample fragments after chromium plating with ion sputtering and to perform compositional tests. Because the sample was fragile, the corrosion layer and cross section of the sample surface were not polished. The voltage was set to 10 kV, and the working distance varied from 4.0 to 6.4 mm under vacuum conditions. The test results included secondary electron images and backscattered electron images.

X-ray diffraction analyses (XRD)

A Bruker D8 Advance X-ray diffractometer (Germany) was used to study the sample corrosion layer. The maximum voltage of the instrument was 60 kV, the maximum tube current was 80 mA, the optical tube power was 2.2 kW (Cu target), and the angle reproducibility was $\pm 0.0001^\circ$. A Vantec 500 two-dimensional surface detector with a test spot diameter of 0.5 mm and an integration time of 300 s was used.

Fluorescent inverted microscope (FIM)

A Japanese Keyence BZ-X800E inverted fluorescence phase contrast microscope configured with three different filters, DAPI-V, GFP and TRITC, was used to test the corrosion layer of the sample. The transmittable light source power was 3.7 W, and the fluorescent fall-out light source power was 40 W.

Attenuated total reflectance-fourier transform infrared spectroscopy (ATR-FTIR)

An American Thermo Scientific Nicolet iS50 Fourier infrared spectrometer was used to test the corrosion layer of the sample, analyse the functional groups of the corrosion material, and determine the presence of microbial corrosion in the sample [22, 23]. Infrared absorption spectroscopy was used to directly test the corrosion area on the surface of the sample. The test range was 500–4000 cm^{-1} with a spectral resolution better than 0.09 cm^{-1} , and the wavenumber accuracy was better than 0.01 cm^{-1} .

Results and discussion

Optical morphology of the corrosion surface

Figure 3 shows the OM images of the sample surface and cross-section. The glass cross-section in Fig. 3a shows

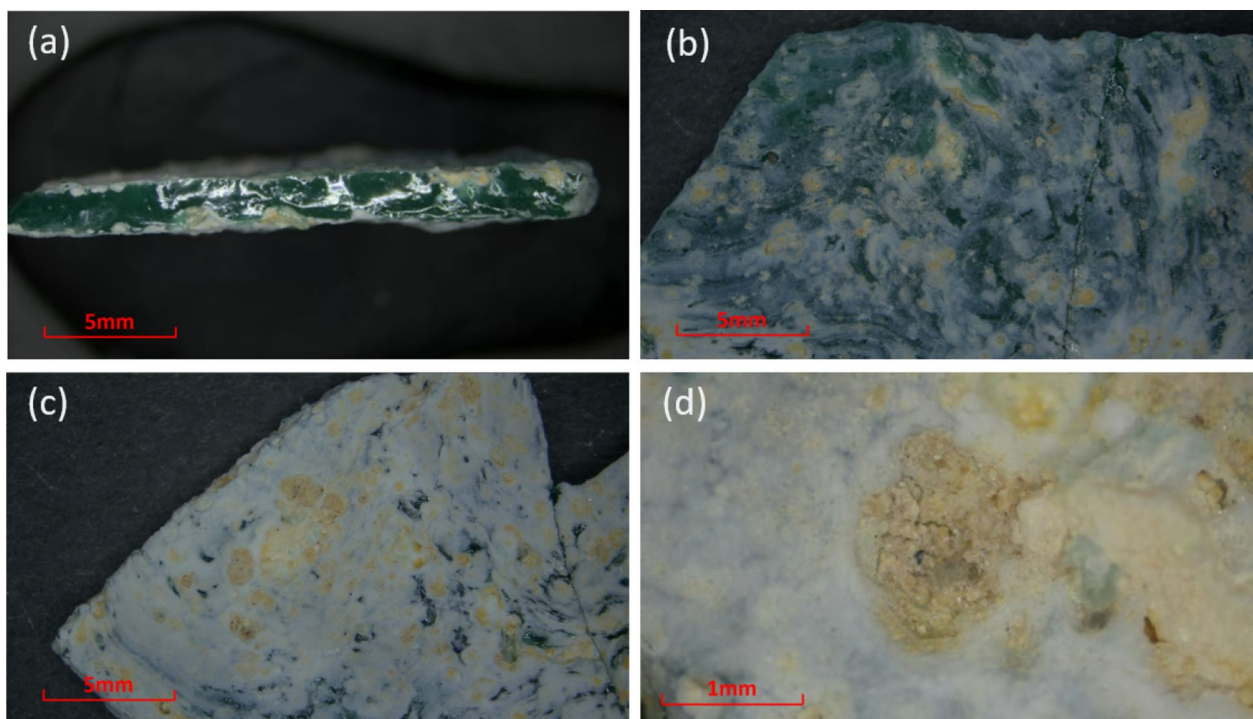


Fig. 3 OM images of the sample, **a** cross-section of the glass sample; **b** and **c** surface corrosion layer; **d** corrosion layer yellow pits

that the sample substrate is blue glass, and the corrosion layer extended from the sample surface to the sample interior, up to approximately 1 mm deep inside the sample. Figure 3b, c shows that a large area of the sample surface was covered with a white corrosion layer, and the corrosion layer was distributed with pits of different sizes and shapes. A yellow corrosion material was generated inside the pits, and the yellow corrosion was in the form of loose particles, as shown in Fig. 3d.

Element distribution on the corrosion surface

XRF mapping was used to test the corrosion layer and determine the compositional distribution of the sample, as shown in the red box in Fig. 4a. The greater the brightness in the figure is, the higher the element content. The distribution of Si indicated in Table 1; Fig. 4b shows that the framework of the structural unit connected at the same angle as the [SiO₄] tetrahedra of the lead-barium glass was corroded, with obvious corrosion pits on the surface. The contents of Pb, Si and Cu in the yellow area inside the corrosion pits had decreased significantly;

however, the accumulated and aggregated Al, Fe, K and Ti showed the same morphology as the corrosion pit. Moreover, the Ba and S contents in the yellow area at the edge of the corrosion pit shown in the yellow circle of 4a were higher, indicating that the accumulation and aggregation of these two elements were consistent in the corrosion pit.

Microstructure and composition of the corrosion layer

To analyse the differences in micromorphologies and compositions of the different areas, the surface and cross-section of the lead-barium glass sample were studied with SEM-EDX, and the results are shown in Fig. 5; Table 2. The micrographs for different areas on the surface of the sample in Fig. 5 showed that there were curly layers in the areas with mild corrosion (Fig. 5a), and the contents of Fe and C were relatively high at P1; compared with the severely corroded area with obvious stratification and circular stripes (Fig. 5b, c), the content of Ba was higher at P2 on the relatively flat surface and approached 10.0%, while the contents of Pb and Ba were

Table 1 Average contents of the chemical elements in the red box area of the sample surface in Fig. 4a (wt%)

Elements	Na ₂ O	MgO	Al ₂ O ₃	SiO ₂	K ₂ O	CaO	TiO ₂	Fe ₂ O ₃	CuO	PbO	SO ₃	BaO	ZnO	SrO
	0.13	0.43	8.01	63.8	0.37	2.83	0.25	0.87	0.52	20.75	0.29	1.51	0.05	0.12

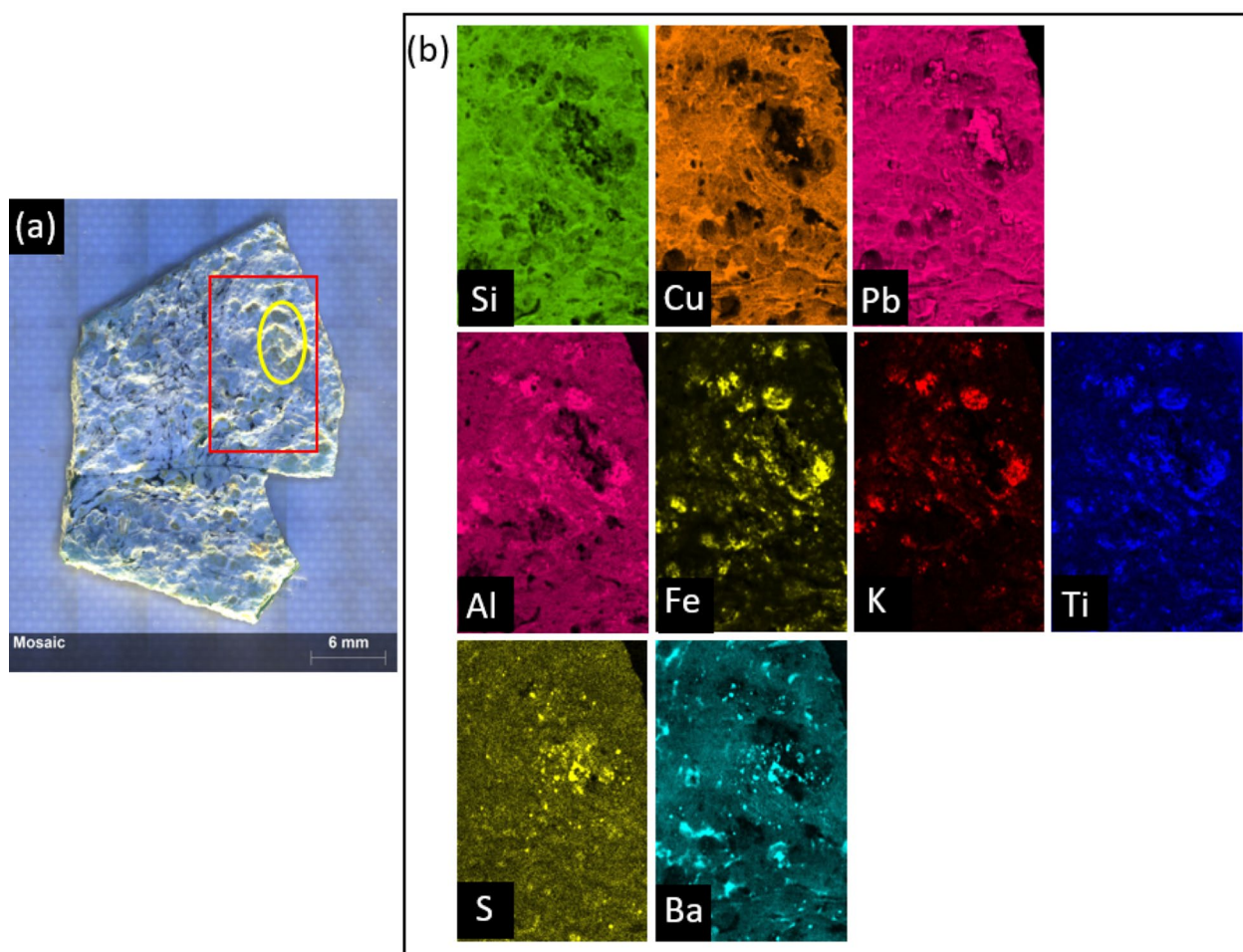


Fig. 4 a XRF analysis area; b element distribution in the analysed area

lower and the content of Si was higher at P3 in the adjacent striated stratification. Furthermore, in Fig. 5d, there were many cracks with widths of 3 μm on the corrosion surface, in which a large number of white particles with obvious contrast were distributed. At P4, the contents of Pb, P and Cl were 71.60%, 4.16% and 2.04%, respectively, and the Pb and P ions were dissolved and obviously dispersed. The microarea XRD results indicated that PbCO_3 was formed on the surface (Fig. 6a).

SEM-EDX was used to observe the cross-sectional morphology of the sample, and the results are shown in Fig. 7; Table 3. The corrosion degree of the sample decreased gradually from the surface to the interior. The corrosion of the lead-barium glass began with a change in the lamellar curly layer on the surface (Fig. 7a). The contents of metal oxides such as PbO , Na_2O and MgO gradually decreased, while the contents of Ba and S increased to match the highest contents of Ba and S in the pit, which were 37.13% and 3.75%, respectively (P10). A comparison of the microstructure of the corrosion pit surface

and its interior showed that the corrosion surface formed a circular stripe with obvious stratification (Fig. 7b, c); the pits were semicircular, and the internal particles were obviously separated (Fig. 7d, e). The BaS_2 crystalline particles formed in the pits were analysed by XRD (Fig. 6b).

The morphologies of the corrosion pits formed in the cross section of the sample were observed (Fig. 7d). The contents of Na, K, Al, Si and other elements in the corrosion pits were low, but the contents of S and Ba were high. The source of S in the newly generated BaS_2 is worthy of further research.

The element P11 in the crack was tested, and there was a high content of P in the crack. The microarea XRD diffraction pattern showed that there was brushite [$\text{CaHPO}_4(\text{H}_2\text{O})_2$] in the corrosion layer (Fig. 6a). Additionally, there was Cl in the sample; since Cl^- is an active anion with a small radius and strong penetration, it was likely to cause crack corrosion [24]. The XRD diffraction pattern revealed the presence of $\text{Pb}(\text{OH})\text{Cl}$ in the corrosion layer (Fig. 6a), indicating that the reaction of

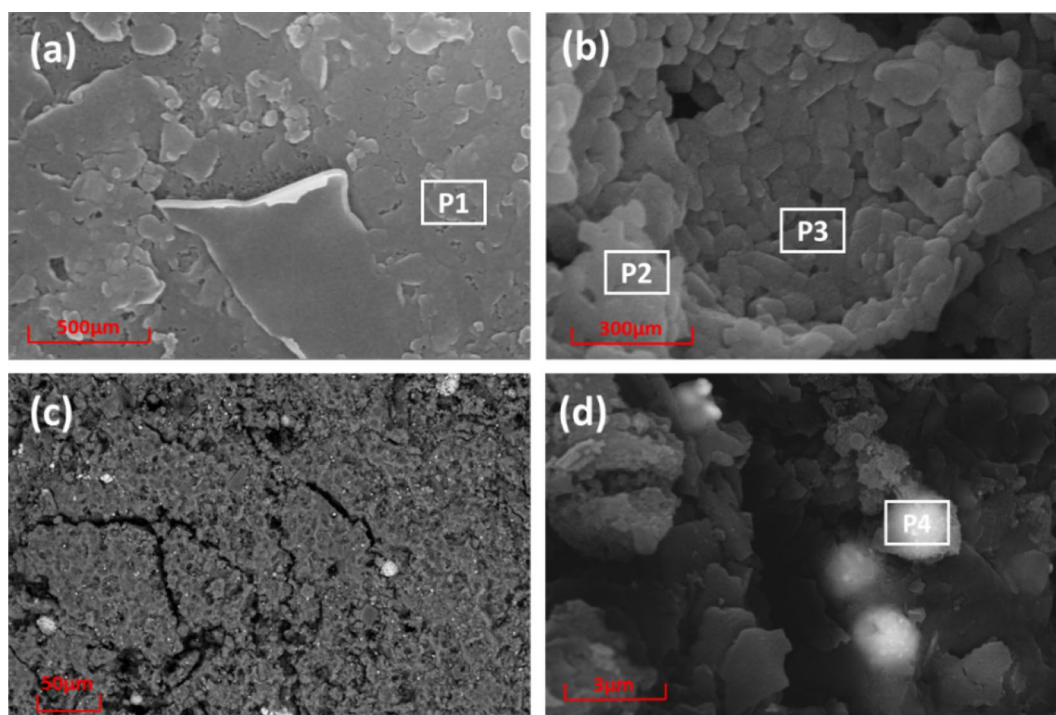


Fig. 5 SEM images of the corrosion surface in the sample, **a** curled layered corrosion; **b** circular striated corrosion; **c** layered corrosion; **d** cracking

Table 2 Elemental compositions at different locations in Fig. 5 (wt%)

Position No.	C	O	Na	Mg	Al	Si	P	S	Cl	Ca	Ti	Fe	Cu	Ba	Pb
P1	3.02	34.42			2.39	14.61	1.94	0.73		0.94	1.96	1.51			38.47
P2		27.81	1.25		1.11	19.05			1.81	0.7			1.64	10	36.63
P3		48.25	0.15	0.34	3.13	37.52	0.28	0.45		1.64			0.46	0.51	7.26
P4		16.31			0.67	3.69	4.16		2.04	0.54	0.28	0.7			71.6

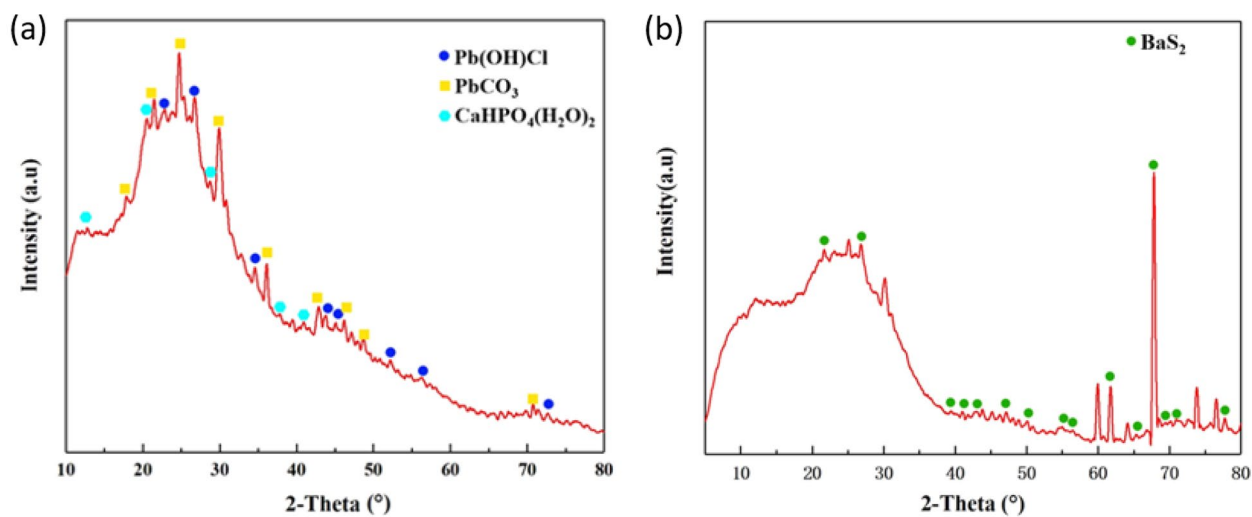


Fig. 6 **a** XRD spectrum of the white corrosion layer on the surface; **b** XRD spectrum recorded for the yellow corrosion layer on the surface

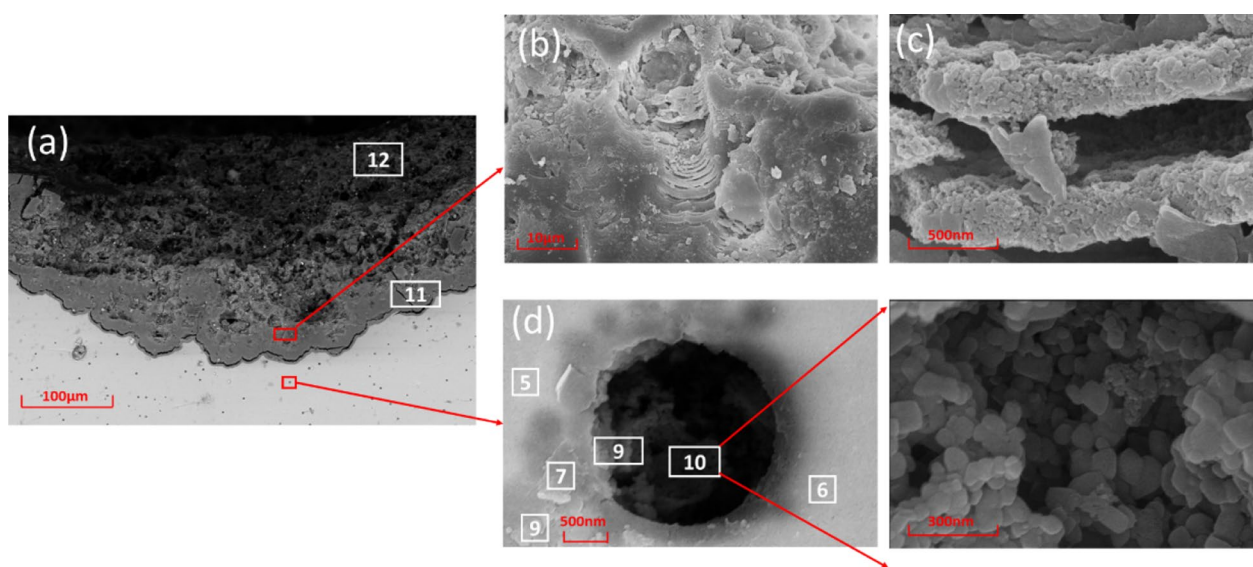


Fig. 7 a SEM image of the cross section of the sample; b, c corrosion in the form of layered circular stripes in the surface layer; d and e phase separation of the corrosion pits inside the sample and particle phase separation inside the pits

Table 3 Chemical compositions at the marked positions in Fig. 7 (wt%)

Position No.	C	O	Na	Mg	Al	Si	P	S	Cl	K	Ca	Ti	Fe	Cu	Ba	Pb
P5		27.24	1.59	0.24	0.97	18.37			1.86	0.17	0.58		0.34	1.48	9.26	37.9
P6		27.8	1.29		0.98	18.55		0.63	1.73		0.58				10.7	37.74
P7		28.42	0.96	0.23	1.32	16.95		1.76	1.15		0.68			1.46	13.82	33.25
P8		29.56	0.89		1.62	17.68		2.14	1.16		0.72				15.51	30.72
P9		23.16			0.51	10		3.37	0.77						37.45	24.74
P10		23.78	0.39		0.55	9.66		3.75	0.74	0.16	0.47		1.15	37.13		22.24
P11		29.6			2.68	16.38	2.19		0.84		1.06	2.2	1.67			43.36
P12	7.87	53.82			3.24	25.09					1.48		0.59		0.66	7.25

Cl^- with Pb^{2+} generated $\text{Pb}(\text{OH})\text{Cl}$ and other products, which existed in the glass corrosion and cracks.

Fluorescence-generating reactions and infrared spectra of the corroded surfaces

The source of S in the corrosion product BaS_2 is unknown, the buried soil environment of the sample was complex and changeable, and there were microorganisms. It is speculated that the S came from microbial metabolites. To verify the existence of microbial corrosion, FIM was used to look for fluorescence from the surface of the corroded area. The results showed that the uncorroded area did not generate a fluorescence image upon excitation at 395 nm, 470 and 545 nm, while the corroded area showed obvious blue, green and red fluorescence with the same excitation light; the green and red fluorescence was significant in some areas with severe

corrosion (Fig. 8c, d). The materials in the corrosion area exhibited self-excitation.

Further studies of the micromorphology and fluorescence distribution in the cross section of the corroded glass showed that there were tadpole-shaped corrosion pits on the inner surface of the sample (Fig. 9), and this area exhibited obvious self-excited fluorescence (Fig. 9b, c), which was presumed to be related to microorganisms with caudal flagella.

ATR-FTIR was used to test the corrosion area, and the resulting IR spectra are shown in Fig. 10. The ATR-FTIR results indicated the presence of a biofilm and the presence of S-H bonds on the corroded surfaces of the lead-barium glass. The spectral band located between 1178 and 1050 cm^{-1} arose from C–O–C skeletal vibrations or S–O stretching vibrations (Fig. 10a); the peak at 1646 cm^{-1} was the amide I band, which results from a C=O stretching vibration, and the peak at 1542 cm^{-1}

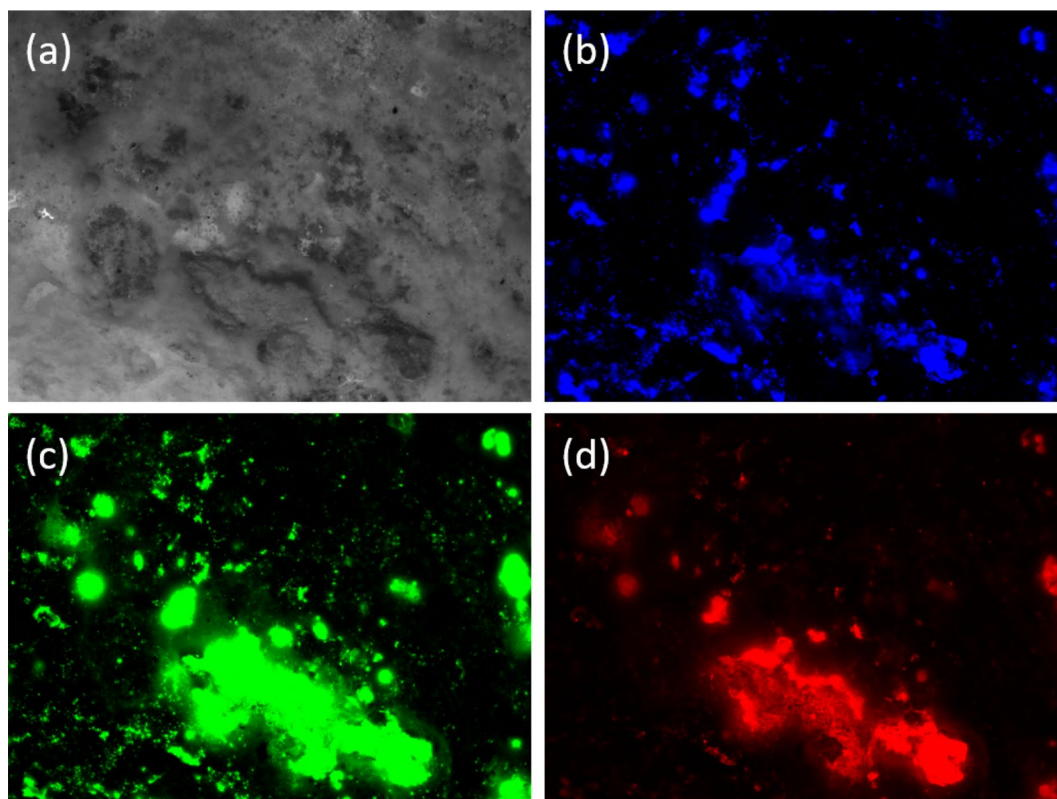


Fig. 8 Fluorescence from the corroded areas of the sample, **a** image of the corroded area without an excitation light source; **b** fluorescence from the sample with excitation at 395 nm; **c** fluorescence from the sample with excitation at 470 nm; **d** fluorescence from the sample with excitation at 545 nm

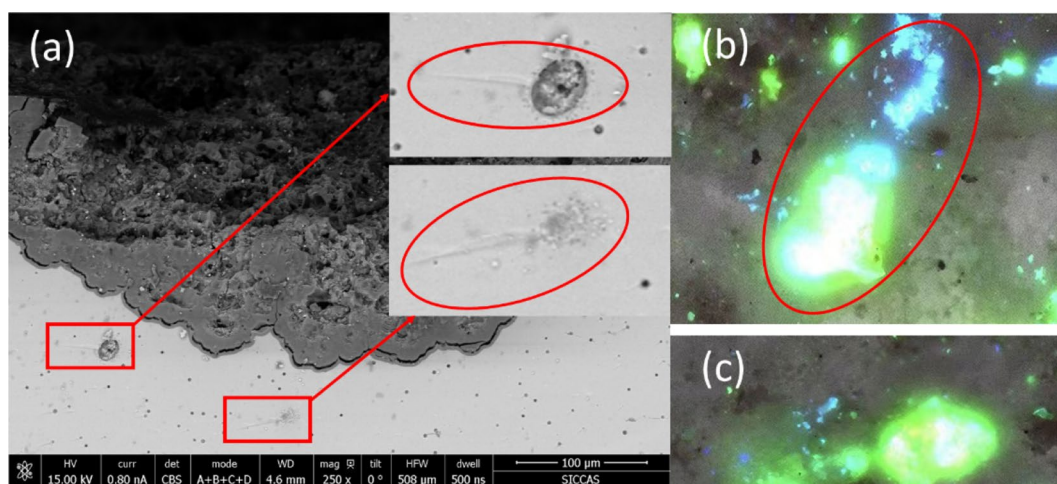


Fig. 9 **a** Cross-sectional SEM-EDX image of the sample; **b** and **c** tadpole-shaped fluorescence

was the amide II band, which results from an N-H bending vibration and C–N stretching vibration (the amide I and II bands are characteristic spectral bands of proteins) (Fig. 10b); S–H stretching vibration peaks

were at 1950–2260 cm^{-1} (Fig. 10c); $-\text{CH}_3$ asymmetric and symmetric stretching vibration peaks were at 2960 cm^{-1} and 2875 cm^{-1} , and $-\text{CH}_2$ asymmetric

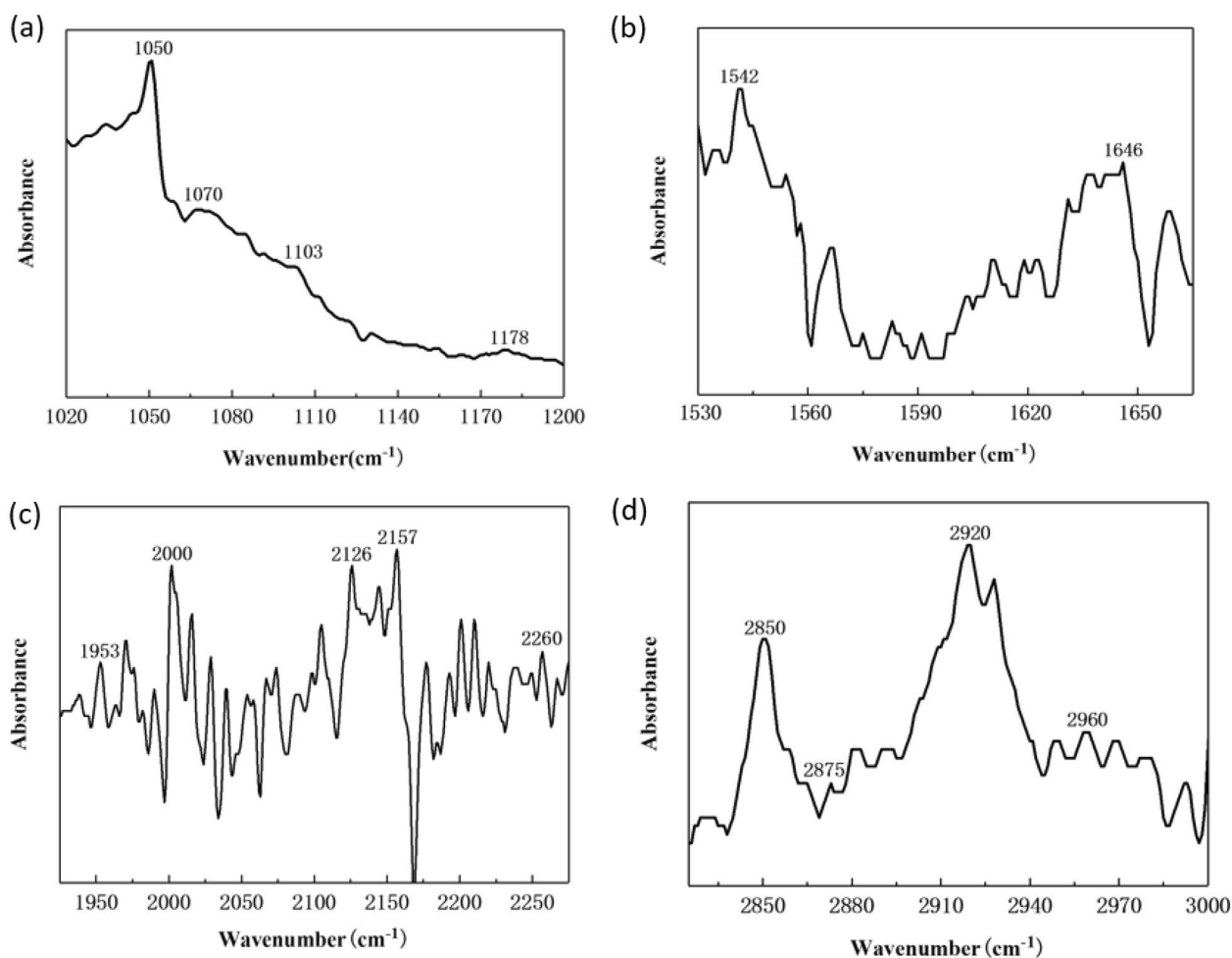


Fig. 10 Infrared spectra of the corrosion layer, **a** C–O–C skeleton vibrational absorption band or S–O stretching peak; **b** amide I and amide II stretching vibration peak; **c** C–H stretching vibration peak; **d** $-\text{CH}_3$ asymmetric and symmetric stretching vibration peak and $-\text{CH}_2$ asymmetric and symmetric stretching vibration peak

and symmetric stretching vibration peaks were at 2920 cm^{-1} and 2850 cm^{-1} (Fig. 10d).

Based on the fluorescence images, morphological characteristics and infrared functional group results described above, it is speculated that microbial corrosion products were present on the surface of the sample. The sample was buried in soil containing many microorganisms for a long time. The pH of the tested soil ranged between 7 and 8, which is the right pH for bacteria, and under anaerobic conditions, silicate bacteria corrode minerals and sulfate-reducing bacteria. Silicate bacteria are microorganisms that dissolve the insoluble potassium and phosphorus salts of silicate minerals, and their metabolic processes produce organic acids, amino acids, polysaccharides and other substances. Currently, the corrosion mechanisms suggested for silicate bacteria include contact between the bacteria and the ore as well as the production of special enzymes that destroy

the crystalline structures of the ores or the metabolites of the bacterial production process to decompose the ore and the surfaces via the physical and chemical contact exchange [25–27]. Sulfate-reducing bacteria are the most important bacteria operating under anaerobic conditions; they are obligate anaerobic gram-negative bacteria, single celled, colourless and spore free, with single flagella movements, and a metabolism that produces high concentrations of hydrogen sulfide [28, 29]. Therefore, it is speculated that the microbial corrosion of the sample may have been caused by these two bacteria. The corrosion processes of specific microorganisms will be demonstrated with experimental simulations in the future.

Corrosion model for the lead-barium glass

Based on the experimental test results described above, it was determined that the corrosion mechanisms for the lead-barium glass included microbial corrosion,

surface chemical corrosion and crack corrosion. Among them, the H_2S and CO_3^{2-} produced by microorganisms undergo chemical reactions with barium ions and lead ions, and chemical changes are included in microbial corrosion. The corrosion models were designed according to the different conditions.

First, the lead-barium glass sample showed surface corrosion and changes in the chemical structures, and the accumulation of the corrosion products was also selective and directional. The aqueous environment of the soil led to dissolution of the silica network, which underwent a hydrolysis reaction to generate $-Si-OH$, which decreased the pH of the sample surface and promoted the formation of corrosion products on the sample surface [30]. Additionally, silicate bacteria destroyed the network structure of the glass, leading to decomposition of the glass skeleton, rapid dissolution of metal oxide ions containing K, Fe, Al and Ti, and obvious circular corrosion pits, while the acidic H_2S produced by the anaerobic silicate-reducing bacteria reacted with Ba ions to generate BaS_2 , which accumulated inside the corrosion pits (Fig. 11).

On the sample surface, the weak acids provided by bio-corrosion, such as carbonic acid, or the acids contained in the soil, especially under anaerobic conditions, played an essential role in corroding the lead-barium glass; the weak acids in the environment reacted with the Pb^{2+} ions

dissolved in the glass to form a slab of sparse $PbCO_3$ (Fig. 12).

As for the cracks in the corroded surface of the sample, Cl^- easily penetrated the glass, gathered in the cracks of the corroded layer and reacted with Pb^{2+} dissolved from the glass to generate $Pb(OH)Cl$. Additionally, HPO_4^{2-} from the soil reacted with the Ca^{2+} dissolved from the glass to generate $CaHPO_4(H_2O)_2$. The corrosion products accumulated in the cracks, which resulted in crack corrosion of the sample (Fig. 13), and the cracks gradually expanded.

Conclusions

Based on the X-ray fluorescence spectroscopy, scanning electron microscopy-energy spectroscopy, microarea X-ray diffraction, fluorescence microscopy and Fourier infrared spectroscopic analyses, it was determined that the corrosion products on the lead-barium ancient glass excavated from Yaozhuang Cemetery in the Liuhe District, Nanjing, included newly generated $PbCO_3$, $Pb(OH)Cl$, $CaHPO_4(H_2O)_2$ and BaS_2 . The forms of corrosion included microbial corrosion, surface chemical corrosion and crack corrosion.

Furthermore, three different corrosion models were built by identifying the corrosion products and types. First, it is speculated that the metabolites of the microorganisms in the buried soil accelerated the destruction of

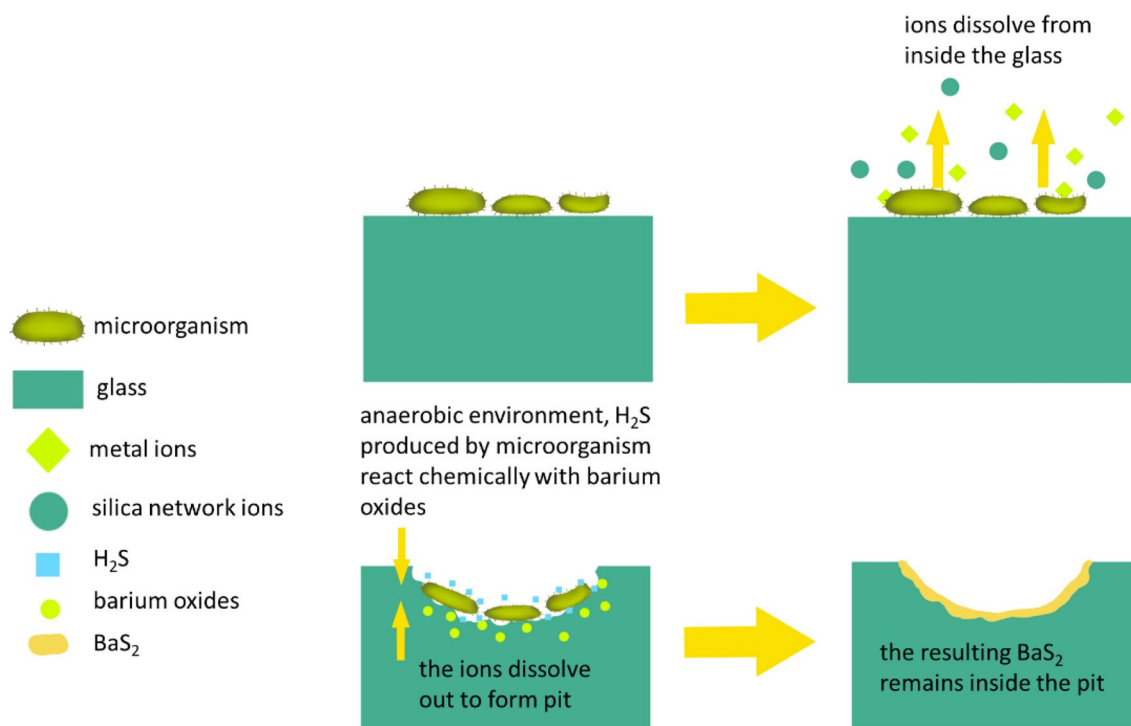


Fig. 11 Formation of corrosion pits and BaS_2

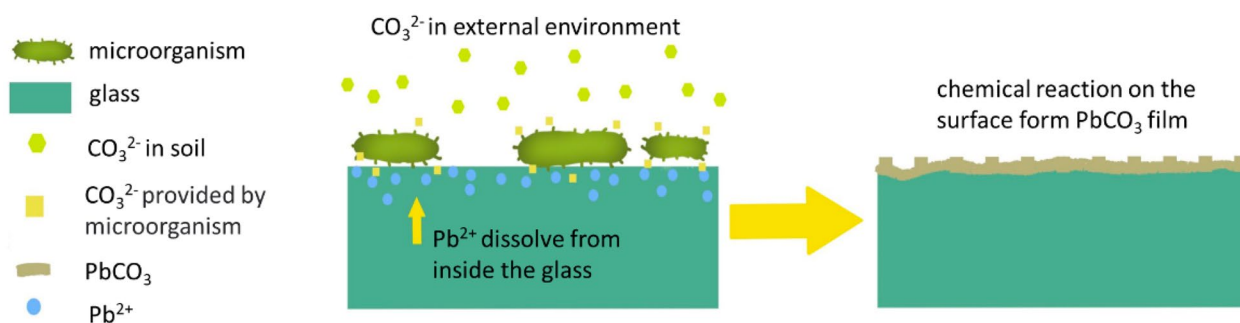


Fig. 12 Formation of PbCO_3 on the surface

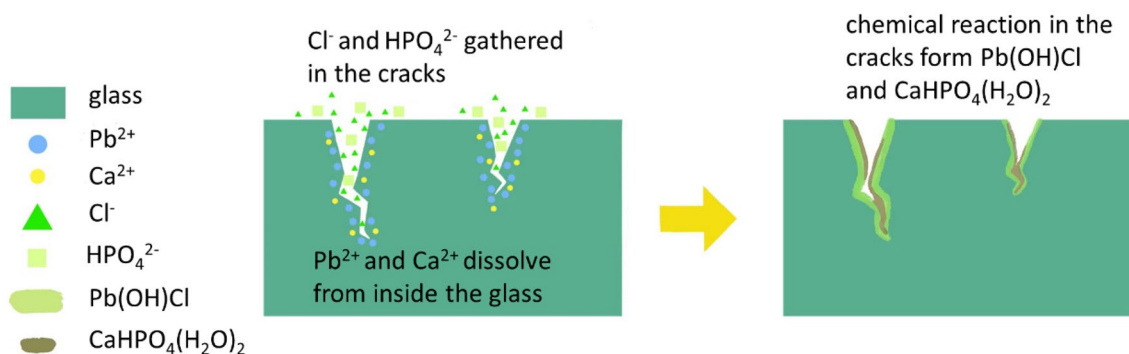


Fig. 13 Crack corrosion process

the glass network, formed corrosion pits, and produced H_2S in the anaerobic environment that reacted with the Ba elements from the glass; the carbonic acid in the buried soil also reacted with the Pb^{2+} from the glass to produce white lead carbonate. Finally, in the corroded crack areas, Cl^- and HPO_4^{2-} from the buried environment accumulated and penetrated deep into the corrosion cracks to generate Pb(OH)Cl and $\text{CaHPO}_4(\text{H}_2\text{O})_2$, which accelerated the crack corrosion. This study provides vital reference value for research on excavated glass relics and serves as a preliminary basis for research on the conservation of glass artefacts.

Acknowledgements

Not applicable.

Author contributions

KZ and WY carried out the experiments and wrote the first draft of the manuscript, JZ designed the experiments and performed the analyses, JW provided the experimental samples, and XY and HL performed the analyses. All coauthors discussed the results and commented on the manuscript. All authors reviewed and edited the final manuscript. All authors read and approved the final manuscript.

Funding

The authors gratefully acknowledge financial support from the National Natural Science Foundation of Shanghai in China (No. 20ZR1422800, No.23ZR1421000) and the Key Program of the National Natural Science Foundation of China (No. 51732008).

Availability of data and materials

All data generated or analysed during this study are included in this published article (and its supplementary information files).

Declarations

Competing interests

The authors declare that they have no competing interests.

Received: 9 December 2022 Accepted: 8 April 2023

Published online: 20 April 2023

References

- Shangguan B. Historical exploration of glass craft. *Art Res.* 1960(01):38–41.
- Gan FX. Origin and development of ancient Chinese glasses. *Chin J Nat.* 2006(04):187–193.
- Gan FX, Cheng HS, Li QH. Origin of Chinese ancient glasses—study on the earliest Chinese ancient glasses. *Sci. China Ser E.* 2007(03):382–391.
- Fu XF, Gan FX. Chemical composition analysis of some ancient glasses unearthed from southern and southwestern China. *Sci Conserv Archaeol.* 2006. <https://doi.org/10.16334/j.cnki.cn31-1652/k.2006.04.002>.
- Henan Provincial Institute of Cultural Relics and Archaeology, Sanmenxia City Cultural Relics Task Force. *The spring and autumn tomb of zhechuan xiasi.* Beijing: Cultural Relics Press; 1991.
- Gan FX, Zhao HX, Li QH, et al. Technological analyses on ancient glass of the Warring States period in Hubei Province. *Jiangnan Archaeol.* 2010;02:108–16.

7. Qin Y, Wang YH, Chen X. The research of burning ancient chinese lead-barium glass by using mineral raw materials. *J Cult Herit.* 2016;21:796–801. <https://doi.org/10.1016/j.culher.2016.04.003>.
8. Tournie A, Ricciardi P, Colombari PH. Glass corrosion mechanisms: a multiscale analysis. *Solid State Ion.* 2008;179:2142–54. <https://doi.org/10.1016/j.ssi.2008.07.019>.
9. Carmona N, Garcia-Heras M, Gil C, et al. Chemical degradation of glasses under simulated marine medium. *Mater Chem Phys.* 2005;94:92–102. <https://doi.org/10.1016/j.matchemphys.2005.04.026>.
10. Bunker BC. Molecular mechanisms for corrosion of silica and silicate-glasses. *J Non-Cryst Solids.* 1994;179:300–8. [https://doi.org/10.1016/0022-3093\(94\)90708-0](https://doi.org/10.1016/0022-3093(94)90708-0).
11. Berger G, Cclaparos C, Guy C, Daux V. Dissolution rate of a basalt glass in silica-rich solutions: implications for long-term alteration. *Geochim Cosmochim Acta.* 1994;58:4875–86. [https://doi.org/10.1016/0016-7037\(94\)90218-6](https://doi.org/10.1016/0016-7037(94)90218-6).
12. Lombardo T, Gentaz L, Verney-Carron A, et al. Characterisation of complex alteration layers in medieval glasses. *Corros Sci.* 2013;72:10–9. <https://doi.org/10.1016/j.corsci.2013.02.004>.
13. Palomar T, Bastidas A, Bastidas DM, et al. Effect of marine aerosols on the alteration of silicate glasses. *J Non-Cryst Solids.* 2017;471:328–37. <https://doi.org/10.1016/j.jnoncrysol.2017.06.013>.
14. Vilarigues M, da Silva RC. Characterization of potash-glass corrosion in aqueous solution by ion beam and IR spectroscopy. *J Non-Cryst Solids.* 2006;352:368–5375. <https://doi.org/10.1016/j.jnoncrysol.2006.08.032>.
15. De Ferri L, Lottici PP, Vezzalini G. Characterization of alteration phases on Potash-Lime-Silica glass. *Corros Sci.* 2014;80:434–41. <https://doi.org/10.1016/j.corsci.2013.11.068>.
16. Coutinho ML, Miller AZ, Gutierrez-Patricio S, et al. Microbial communities on deteriorated artistic tiles from Pena National Palace (Sintra, Portugal). *Int Biodeterior Biodegrad.* 2013;84:322–32. <https://doi.org/10.1016/j.ibiod.2012.05.028>.
17. Portillo MC, Gazulla MF, Sanchez E, et al. A procedure to evaluate the resistance to biological colonization as a characteristic for product quality of ceramic roofing tiles. *J Eur Ceram Soc.* 2011;31:351–9. <https://doi.org/10.1016/j.jeurceramsoc.2010.10.012>.
18. Pinto AMC, Palomar T, Alves LC, et al. Fungal biodeterioration of stained-glass windows in monuments from Belem do para (Brazil). *Int Biodeterior Biodegrad.* 2019;138:106–13. <https://doi.org/10.1016/j.ibiod.2019.01.008>.
19. Rodrigues A, Gutierrez-Patricio S, Miller AZ, et al. Fungal biodeterioration of stained-glass windows. *Int Biodeterior Biodegrad.* 2014;90:152–60. <https://doi.org/10.1016/j.ibiod.2019.01.008>.
20. Branysova T, Demnerova K, Durovic M, et al. Microbial biodeterioration of cultural heritage and identification of the active agents over the last two decades. *J Cult Herit.* 2022;55:245–60. <https://doi.org/10.1016/j.culher.2022.03.013>.
21. Shirakawa MA, John VM, Mocelin A, et al. Effect of silver nanoparticle and TiO2 coatings on biofilm formation on four types of modern glass. *Int Biodeterior Biodegrad.* 2016;108:175–80. <https://doi.org/10.1016/j.ibiod.2015.12.025>.
22. Wenning M, Theilmann V, Scherer S. Rapid analysis of two food-borne microbial communities at the species level by Fourier-transform infrared microspectroscopy. *Environ Microbiol.* 2006;8:848–57. <https://doi.org/10.1111/j.1462-2920.2005.00971.x>.
23. He HJ, Sun DW. Microbial evaluation of raw and processed food products by Visible/Infrared, Raman and fluorescence spectroscopy. *Trends Food Sci Technol.* 2017;46:199–210. <https://doi.org/10.1016/j.tifs.2015.10.004>.
24. Song L, Liu JL, Cui CX, et al. Multi-factor sensitivity analysis of chloride ingress: a case study for Hangzhou Bay Bridge. *Constr Build Mater.* 2022. <https://doi.org/10.1016/j.conbuildmat.2022.127089>.
25. He JQ, Li DY, Zhang XP, et al. Research progress on silicate bacteria. *Southwest China J Agric Sci.* 1999. <https://doi.org/10.16213/j.cnki.scjas.1999.s1.020>.
26. Gu FQ, Wei YI J, XI. Research and progress on soil silicate bacteria. *Chin J Ecol.* 2013;25(05):609–11. <https://doi.org/10.13381/j.cnki.cjm.2013.05.008>. (in Chinese).
27. Sun DS, Chen Y, Cao F. Degradation of bauxite with complicate mineral compositions by microorganisms in culture experiments. *J Mineral Petrol.* 2012;32(03):6–12. <https://doi.org/10.19719/j.cnki.1001-6872.2012.03.002>.
28. Machel HG. Bacterial and thermochemical sulfate reduction in diagenetic settings - old and new insights. *Sediment Geol.* 2001;140:143–75. [https://doi.org/10.1016/S0037-0738\(00\)00176-7](https://doi.org/10.1016/S0037-0738(00)00176-7).
29. Deng Q, Wu X, Wang Y, et al. Activity characteristics of sulfate reducing bacteria and formation mechanism of hydrogen sulfide. *Appl Ecol Environ Res.* 2018;16(5):6369–83. https://doi.org/10.15666/aeer/1605_63696383.
30. Melcher M, Schreiner M. Statistical evaluation of potash-lime-silica glass weathering. *Anal Bioanal Chem.* 2004;379:628–39. <https://doi.org/10.1007/s00216-004-2595-0>.

Publisher's Note

Springer Nature remains neutral with regard to jurisdictional claims in published maps and institutional affiliations.

Submit your manuscript to a SpringerOpen® journal and benefit from:

- Convenient online submission
- Rigorous peer review
- Open access: articles freely available online
- High visibility within the field
- Retaining the copyright to your article

Submit your next manuscript at ► [springeropen.com](https://www.springeropen.com)